PAPER

Check for updates

Anchoring defective metal-free catalysts on montmorillonite nanosheets for tetracycline removal: synergetic adsorption-catalysis and mechanism insights†

Min Li,[a] Xudong Liu,[ab] Zhinan Xie,[a] Chunfang Du ⓘ *[a] and Yiguo Su ⓘ *[a]

A one-step thermal polymerization approach was adopted to combine C_3N_5 with montmorillonite nanosheets (MMT Ns) to form xCN-MMT for the degradation of pollutants in water. Benefitting from the abundant hydroxyl groups on the MMT surfaces, double defects ($-C\equiv N$ and N defects) were introduced in xCN-MMT catalysts to promote the adsorption of tetracycline (TC), peroxymonosulfate (PMS), and oxygen. 10CN-MMT exhibited superior adsorption performance toward TC, with the adsorption capacity being 5.65-fold that of MMT Ns and 2.64-fold that of C_3N_5. Further, 10CN-MMT exhibited better PMS activation performance than MMT Ns and C_3N_5, which could degrade 95% of TC within 120 min. Moreover, the total organic carbon (TOC) removal efficiency of the present system reached 81.1%, and the chemical oxygen demand (COD) decreased from 50.7 to 12.2 mg L^{-1}. The degradation process of TC was characterized using liquid chromatography-tandem mass spectrometry (LC-MS), and a reasonable degradation pathway and catalytic mechanism were given by combining with active species analysis. The toxicological analysis of the degradation products also showed a significant decrease in toxicity. The degradation experiments in different water environments were also simulated, and it was found that 10CN-MMT showed good adsorption effects. This study provides a green metal-free clay-based catalyst and shows good applicability in removing antibiotics.

Environmental significance

Tetracycline (TC) has become the most commonly used antibiotics due to its low cost, wide range of applications, and multiple modes of intake. However, TC causes environmental damage when it enters the ecosystem and cannot be effectively removed by traditional water treatment methods due to its stable structure. Activated peroxymonosulfate (PMS) is a typical advanced oxidation process (AOP) that generates reactive radicals ($\cdot OH$ and $SO_4^{\cdot-}$) by transition metal ions, UV light, heat, and electrochemical processes. However, these methods may lead to the leaching of metal ions and consume large amounts of energy, which results in secondary water pollution. Therefore, we used a one-step thermal polymerization method to combine C_3N_5 with montmorillonite nanosheets (MMT Ns) to form xCN-MMT for the degradation of pollutants in water. 10CN-MMT was able to degrade 95% of TC within 120 min through the synergistic effect of adsorption and degradation. In the 10CN-MMT/PMS system, the total organic carbon (TOC) could reach 81.1%, and the chemical oxygen demand (COD) was reduced from 50.7 mg L^{-1} to 12.2 mg L^{-1}. Therefore, this study not only provides a new idea for the construction of metal-free clay-based catalysts but also provides a green and efficient catalyst for the activation of PMS to degrade antibiotics.

Introduction

Tetracycline (TC) has become the most commonly used antibiotic due to its low cost, wide range of applications, and multiple modes of intake.[1,2] However, TC causes environmental

[a]*Inner Mongolia Key Laboratory of Chemistry and Physics of Rare Earth Materials, School of Chemistry and Chemical Engineering, Inner Mongolia University, Hohhot, Inner Mongolia 010021, PR China. E-mail: cesyg@imu.edu.cn; cedchf@imu.edu.cn; Fax: +86 471 4994375; Tel: +86 471 4994375*

[b]*Department of Chemistry, Baotou Teachers' College, Baotou, Inner Mongolia 014030, PR China*

damage when it enters the ecosystem and cannot be effectively removed by traditional water treatment methods due to its stable structure.[3] Physical methods can be used as a pre-treatment step to reduce the cost of wastewater treatment.[4] Chemical methods can be used to degrade macromolecules into non-toxic or low-toxic small molecules through redox reactions.[5] Activated peroxymonosulfate (PMS) is a typical advanced oxidation process (AOP), which is more suitable for environmental applications due to its high redox potential, long half-life, and wide pH range.[6] Generally, PMS can generate reactive radicals ($\cdot OH$ and $SO_4^{\cdot-}$) by transition metal ions, UV light, heat, and electrochemical processes.[7] However, these methods may lead to the leaching of metal ions and consume large

amounts of energy, which results in secondary water pollution. Thus, it is necessary to explore a metal-free low-cost catalyst that can effectively activate PMS without the help of extra energy sources.

Carbon nitride is a typical metal-free material with high thermal stability, non-toxicity, low cost, and unique electronic properties, which can replace metal-based catalysts for environmental treatment. Carbon nitride with nitrogen functionalities (*e.g.*, –NH$_2$, –NH–) serves as strong Lewis base sites, which are potential ideal sites for metal-based catalysts.[8] Guan *et al.*[9] prepared a variety of C$_3$N$_4$ using different precursors with different catalytic activities for PMS activation, which could remove BPA with 100% efficiency within 15 min. Different preparation processes affect the chemical composition and structure of the catalysts, thus changing the type of active sites. In addition, it has been demonstrated that the nitrogen content can be adjusted to achieve efficient environmental purification and energy conversion.[10] Kumar and coworkers[11] synthesized a novel N-rich polymer carbon nitride material with a stoichiometric ratio of C : N = 3 : 5 (C$_3$N$_5$). Unlike the structure of g-C$_3$N$_4$ in which three heptazine units are linked to the tertiary nitrogen, the two s-heptazine units in the C$_3$N$_5$ polymer are linked together by an azo bond, constituting an utterly new bonding mode.[12] Porous C$_3$N$_5$ exhibited excellent adsorption performance for methylene blue[11] and the adsorption process reached 90% adsorption–desorption equilibrium within only 1 min, achieving adsorption–desorption equilibrium within 10 min. Fu *et al.*[13] prepared piezoelectric-photocatalysts C$_3$N$_5$-*x*-CN for the removal of tetracycline. This catalyst demonstrated excellent efficiency toward tetracycline removal, with a kinetic constant of 0.0342 min^{-1}, which can be further improved in the presence of PMS. The double-defective sites in the catalyst synergistically greatly improved the catalytic activity. These results indicate that C$_3$N$_5$ acts as a promising candidate in various applications, especially in the field of wastewater treatment. However, the activation of PMS by C$_3$N$_5$ alone without the aid of additional energy still faces the problem of low activity, so further modification of C$_3$N$_5$ is needed to improve its catalytic properties.

Montmorillonite (MMT) is a typical water-bearing layered silicate clay mineral and shows strong hydrophilicity due to high charge density on the lamellar surface.[14,15] Thus, MMT can be easily exfoliated into montmorillonite nanosheets (MMT Ns) under external forces characterized by small size, high surface energy, and strong dispersion. In addition, montmorillonite has abundant hydroxyl groups on its surface, and these properties make MMT show great potential in the design and synthesis of novel mineral functional materials.[16,17] Surface hydroxyl groups can not only help to immobilize other nanomaterials to form heterojunctions and improve the mass transfer rate between PMS and contaminants but can also be used to construct defective sites in the composites. Liu *et al.*[18] used MMT as a support material to anchor Co$_x$Mn$_{3-x}$O$_4$ nanoparticles, and the composites showed excellent ability to activate PMS. Zhang *et al.* utilized the abundance of coal gangue surface hydroxyl groups introduced in C$_3$N$_4$ with double nitrogen defects, which could remove 90% of BPA after

activation of PMS within 30 min.[19] Inspired by previous excellent works, the introduction of C$_3$N$_5$ in MMT Ns is likely to show efficient PMS activation performance for the degradation of pollutants in water.

Hence, a series of metal-free catalysts (*x*CN-MMT) based on MMT and C$_3$N$_5$ was prepared for the purpose of efficient PMS activation to degrade TC without the help of additional energy. The catalysts were comprehensively analysed, experimental parameters were optimized, and the reaction mechanism and possible degradation pathways of TC were proposed. This work constructed a novel reaction system for activating PMS without metal catalysts, which provides a new idea for purifying water resources.

Materials and methods

Chemicals

Montmorillonite was purchased from Guzhang Shanlin Shiyu Mineral Products Co., Ltd. 3-Amino-1,2,4-triazole (C$_2$H$_4$N$_4$, ≥96.0%) and tetracycline (C$_{22}$H$_{24}$N$_2$O$_8$, TC) were of analytical grade and purchased from Shanghai Eon Chemical Technology Co., Ltd, China. Peroxymonosulfate (2KHSO$_5$·KHSO$_4$·K$_2$SO$_4$, PMS) was purchased from Meryer Chemical Technology Co., Ltd. Hydrochloric acid (HCl) and absolute ethanol (EtOH) were purchased from Tianjin Fengchuan Chemical Reagent Technology Co., Ltd. Methylene blue (MB), ciprofloxacin (CIP), oxytetracycline (OTC), and 2,4-dichlorophenol (2,4-DCP) were purchased from Shanghai Aladdin Biochemical Technology Co., Ltd. Sodium hydrogen carbonate (NaHCO$_3$), ethanol (C$_2$H$_5$OH, EtOH), sodium hydroxide (NaOH), nitric acid (HNO$_3$), *tert*-butyl alcohol (C$_4$H$_{10}$O, TBA), *p*-benzoquinone (C$_6$H$_4$O$_2$, *p*-BQ), and sodium azide (NaN$_3$, SA) were purchased from Beijing Inno-Chem Science & Technology Co., Ltd. All chemicals were directly used and without further purification.

Preparation of C$_3$N$_5$

The C$_3$N$_5$ (CN) was synthesized by thermal polycondensation of 3-amino-1,2,4-triazole powders. About 1.5 g of 3-amino-1,2,4-triazole powder was dissolved in 30 mL of deionized water and heated in a covered corundum crucible at 550 °C for 4 h with a heating rate of 5 °C min^{-1} in a muffle furnace. The pale yellow C$_3$N$_5$ was obtained after cooling down to room temperature.

Preparation of MMT Ns

The montmorillonite (MMT) was exfoliated by the freezing/thawing-ultrasonic exfoliation method. The MMT suspension (10 g L^{-1}) was prepared by uniformly dispersing the montmorillonite powder into distilled water and stirring it for 3 h at room temperature. The MMT suspension was placed in the ultrasonic cleaner for 10 min and immediately transferred to the freeze drier for a freezing/thawing cycle. The final montmorillonite nanosheets (MMT Ns) were obtained.

Preparation of *x*C$_3$N$_5$-MMT catalysts

*x*C$_3$N$_5$-MMT (*x*CN-MMT) catalysts were prepared as follows: 1.5 g of 3-amino-1,2,4-triazole powders and different amounts

© 2024 The Author(s). Published by the Royal Society of Chemistry

Environ. Sci.: Adv., 2024, **3**, 290–303 | **291**

of MMT Ns (0.5, 0.3, 0.15, 0.1, 0.075, 0.06 or 0.05 g) were mixed thoroughly and dispersed in 30 mL of deionized water. Then, the mixture was heated in a muffle furnace at 5 °C min^{-1} for 4 h at 550 °C. After the samples were naturally cooled down, a series of catalysts were obtained, which were marked as 3CN-MMT, 5CN-MMT, 10CN-MMT, 15CN-MMT, 20CN-MMT, 25CN-MMT, and 30CN-MMT, respectively. To further specify the surface hydroxyl groups of MMT on the catalytic performance, the MMT was calcined at temperatures (700 and 800 °C) for 3 h, respectively. The obtained products were denoted as MMT (700 °C) and MMT (800 °C). 10CN-MMT (700, 800 °C) catalysts were fabricated for comparison, and the preparation procedure was similar to that for xCN-MMT.

Characterizations

The obtained sample's structure was analysed using a Bruker D8 X-ray diffractometer (XRD, Bruker-AXS, Germany) using Cu Kα radiation ($\lambda = 0.1540598$ nm) analysis. The morphologies and lattice fringes of samples were measured using a JEM2100F (Japan) transmission electron microscopy (TEM) imaging. The surface chemical composition and elemental valence of the catalysts were analysed using X-ray photoelectron spectrometer (XPS, ESCALAB 250Xi, Thermo Fisher, USA). Nitrogen absorption–desorption examined the Brunauer–Emmett–Teller specific surface area of the sample (BET Micrometers ASAP 2020). The UV-visible absorption spectra were measured on a spectrophotometer (UH-3900) in the 200–600 nm range. Electron spin resonance (ESR) measurements were performed on a Bruker A300 spectrometer using 5,5-dimethyl-1-pyrroline N-oxide (DMPO) and 2,2,6,6-tetramethyl-4-piperidone (TEMP) as radical scavenging agents. The electron spin resonance spectra (ESR) were performed on a Brooke A300 spectrometer. The electron spin resonance spectra (ESR) were monitored by setting a center field of 323.900 mT, a microwave frequency of 9064.930 MHz, and a power of 0.998 mW. Elemental analysis (EA) was conducted on an elemental analyser (Thermo Scientific FlashSmart, America). Fourier transform infrared (FT-IR) spectra were recorded on a WQ520 spectrophotometer (PerkinElmer, China) with a KBr pellet technique in the 4000–400 cm^{-1} wavenumber range.

Adsorption tests

Adsorption experiments were conducted by dispersing 40 mg of 10CN-MMT in 50 mL of TC solution (50 mg L^{-1}) at room temperature. The adsorption experiments were carried out under continuous stirring. During adsorption, 2 mL of the suspension containing 10CN-MMT and TC was removed every 10 min. The concentration of TC was measured on a UV-Vis spectrophotometer at the wavelength of 357 nm. The adsorption efficiency (%) and adsorption capacity (q_e) were calculated according to eqn (1) and (2), respectively.

$$\text{Adsorption efficiency } (100\%) = \frac{(C_0 - C_t)}{C_0} \times 100\% \quad (1)$$

$$q_e = \frac{(C_0 - C_e)V}{M} \quad (2)$$

C_0 is the initial concentration of TC, M is the mass of the adsorbent, and C_t and C_e are the concentrations at time t and adsorption equilibrium, respectively.

Catalytic tests

The catalytic test was carried out in a 50 mL beaker by dispersing 40 mg of catalyst into 50 mL of TC solution (50 mg L^{-1}). The reaction system was stirred continuously at room temperature for 60 min to reach the adsorption–desorption equilibrium. Then, PMS (0.30 mmol L^{-1}) was poured into the above solution to touch off the reaction. 2 mL of the suspension was taken out every 10 min, and the solids were removed using a 0.22 μm filter. The supernatant was quenched immediately with sodium nitrite.

The degradation intermediates of TC were analysed using the liquid chromatography-quadrupole time-of-flight mass spectrometer (LC-Q-TOF-MS), which was equipped with Thermo Fisher. A total organic carbon (TOC) analyser (Shimadzu TOC, Japan) was used to analyse the mineralization efficiency. A chemical oxygen demand (COD) analyser (CBPN-401C/D, COD, Guangzhou) used a closed digestion colorimetric method to measure the amount of organic matter in water.

Recycling tests

10CN-MMT, after adsorption of TC, was immersed into NaOH solution (0.1 mol L^{-1}), heated, and stirred at 60 °C for 60 min. Then, the adsorbent was filtered, washed with distilled water to neutrality, and subjected to a freezing/thawing cycle in a freeze drier for the next adsorption test (alkali-heat sample).

Results and discussion

Structural and morphological characterization of catalysts

Fig. 1a shows the XRD patterns of C$_3$N$_5$, MMT, and 10CN-MMT. The synthesized C$_3$N$_5$ has two distinct diffraction peaks at $2\theta = 13.4°$ and $27.7°$, related to the (100) and (002) planes, respectively. The peak located at $2\theta = 13.4°$ belonged to in-plane structure ordering, and the strong peak at $2\theta = 27.7°$ is attributed to the interlayer stacking peak of the aromatic system in graphitic materials.[20,21] Furthermore, elemental analysis for the C$_3$N$_5$ sample confirmed that the percentages of C and N were 36.5% and 59.8%, respectively (Table S1†). The atomic ratio of C/N was thus determined to be 0.610, close to the theoretical value (0.60), confirming the formation of C$_3$N$_5$.[21] The XRD pattern of MMT matched well with the standard PDF card (JCPDS card no. 13-0259). In the XRD pattern of 10CN-MMT, the diffraction peaks at 19.7°, 27.7°, and 35.1° were assigned to the characteristic peaks of C$_3$N$_5$ and MMT, respectively. Fig. 1b displays the XRD patterns of 10CN-MMT with different weight ratios of MMT to C$_3$N$_5$. It is found that the intensity of the diffraction peaks attributed to MMT in xCN-MMT increased with the increase in MMT contents.

The FT-IR spectra of MMT, C$_3$N$_5$, and 10CN-MMT are shown in Fig. 1c. In the spectrum of C$_3$N$_5$, the peak located at 3167 cm^{-1} is attributed to the surface residual –NH$_2$ and/or –OH stretching. The peaks at 1641, 1462, 1413, 1323, and
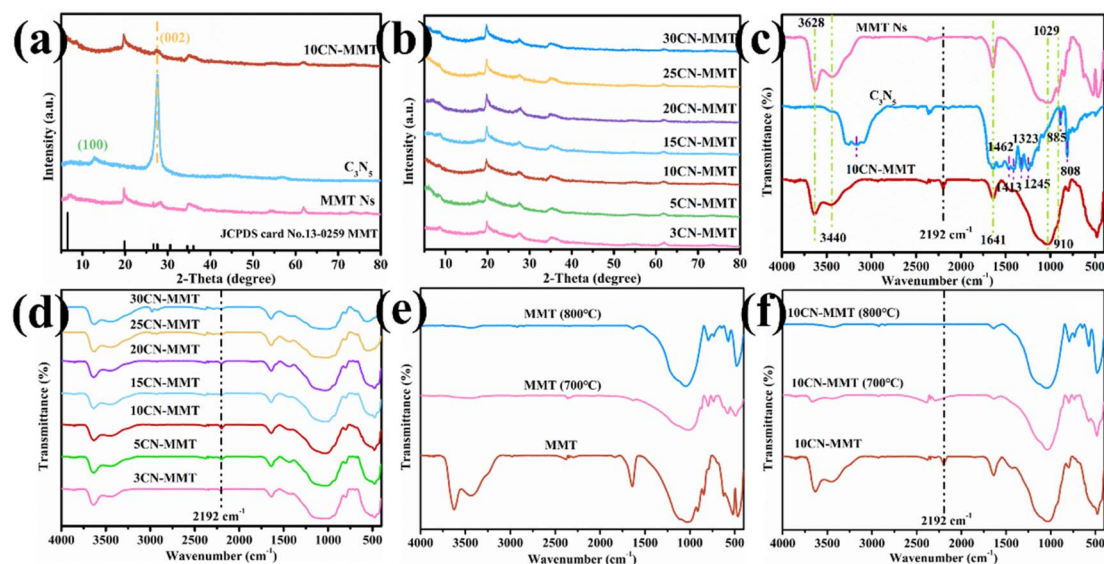
Fig. 1 XRD patterns of MMT, C_3N_5, and 10CN-MMT (a) and xCN-MMT samples with various weight ratios of C_3N_5 to MMT (b). FT-IR spectra of MMT, C_3N_5, and 10CN-MMT samples (c). FT-IR spectra of xCN-MMT samples (d). FT-IR spectra of MMT, MMT (700 °C), and MMT (800 °C) (e). FT-IR spectra of 10CN-MMT, 10CN-MMT (700 °C), and 10CN-MMT (800 °C) (f).

1245 cm^{-1} are related to the triazine ring stretch. The peaks at 885 and 808 cm^{-1} are ascribed to the bending vibrations of N–H. These results are in good agreement with previous reports.[22,23] The absorption peak at 3628 cm^{-1} is attributed to the hydroxyl stretching vibration of structural water in the MMT lattice. In the spectrum of MMT Ns, the absorption peak at 3440 cm^{-1} belonged to the hydroxyl stretching vibration of adsorbed water in the MMT interlayer. The absorption peak at 1641 cm^{-1} is the hydroxyl bending vibration of adsorbed water molecules. The broad absorption peak at 1029 cm^{-1} corresponds to the Si–O–Si stretching vibrations in the MMT lattice. The weak absorption peak at 910 cm^{-1} belongs to the bending vibration of the octahedral hydroxyl group in MMT.[24,25] The spectra of 10CN-MMT showed the characteristic peaks of both C_3N_5 and MMT, indicating the co-presence of C_3N_5 and MMT. A new vibration peak at 2192 cm^{-1} is observed for 10CN-MMT, being attributed to the cyano group (–C≡N),[19,26] suggesting that the –C≡N group was introduced during the thermal polymerization process in the presence of MMT. Furthermore, the FT-IR spectra of all xCN-MMT samples and the effect of the MMT hydroxyl group were investigated. As shown in Fig. 1d, all xCN-MMTs catalysts exhibit similar FT-IR spectra with a distinct –C≡N peak at 2192 cm^{-1}. In order to further investigate the role of hydroxyl groups on the MMT surface, MMT was calcined at different temperatures and used to synthesize CN-MMT catalysts. As shown in Fig. 1e, the characteristic peaks of hydroxyl groups on the MMT surface at 3628 and 3440 cm^{-1} disappeared after calcination at 700 and 800 °C, indicating that the surface hydroxyl groups were removed. Interestingly, the –C≡N of 10CN-MMT (700 °C) and 10CN-MMT (800 °C) catalysts also disappeared (Fig. 1f). The results further indicated that the MMT surface hydroxyl groups have an important effect on the generation of –C≡N groups in the catalysts.

The chemical composition and surface characteristics of C_3N_5, MMT Ns, and 10CN-MMT were investigated by XPS measurement. As shown in Fig. 2a, the XPS spectra of C_3N_5 contained predominantly C, N, and a small amount of O, which could be attributed to atmospheric moisture or CO_2 adsorbed on the C_3N_5 surface.[21] The signals of Al, Si, C, N, and O elements were all observed in the full survey XPS spectra of 10CN-MMT. As shown in Fig. S1,† the characteristic peaks of Al 2p and Si 2p orbitals were shifted from 75.98 and 104.1 eV in MMT Ns to 76.15 and 104.2 eV in 10CN-MMT, respectively. It is well known that the electronegativity of an atom affects the electron density around it. The decrease in electron density reduced the electron shielding effect and thus enhanced the binding energy.[27] The electronegativity of C and N atoms differed from that of Si and Al atoms. Thus, the strong interfacial interactions upon the binding of MMT Ns and C_3N_5 shift the characteristic peaks toward higher binding energies.[28]

The high-solution C 1s XPS spectra of C_3N_5 and 10CN-MMT are displayed in Fig. 2c. In the C 1s spectrum of C_3N_5, four peaks located at 285.4, 286.5, 288.6, and 289.6 eV were attributed to indeterminate carbon (C1), C–NH_x group (C2), carbon atoms bonded by the three N-adjacent bonds (C3) and =C–NH_2 groups (C4), respectively.[29] As for the C 1s spectra of 10CN-MMT, it is seen that the proportion of C3 peaks was significantly reduced, which indicated that the N_2–C=N– structure at the tertiary carbon position was disrupted, and more defects were formed.[30] Meanwhile, the intensity of the C1 peak significantly increased, indicating that more indeterminate carbon was formed, possibly due to the formation of N defects.

As shown in Fig. 2b, the peaks in the N 1s spectra located at 399.3 eV (N1) and 400.8 eV (N2) were attributed to C=N–C group nitrogen atoms and bridging nitrogen atoms (C–N=N–C) or amino nitrogen atoms (C–NH_2), indicating the presence of
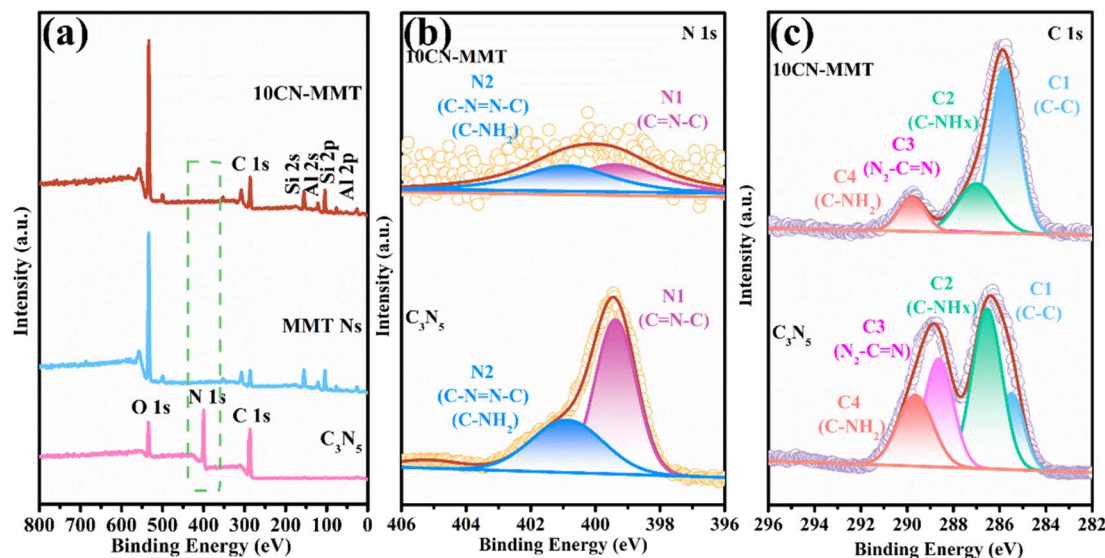
© 2024 The Author(s). Published by the Royal Society of Chemistry

Environ. Sci.: Adv., 2024, **3**, 290–303 | **293**

Fig. 2 The full survey XPS spectra (a), N 1s spectra (b), and C 1s spectra (c) of C_3N_5 and 10CN–MMT.

triazine and triazole groups in all C_3N_5-based materials. However, in the 10CN-MMT sample, a significant weakening of the N 1s signal is observed, which might be related to the presence of N defects. Besides the decrease in the N1 peak intensity, the peak intensity ratio of N1/N2 simultaneously decreased from 1.68 for C_3N_5 to 1.03 for 10CN-MMT, suggesting that the defects in the sample might have eliminated part of the triazine structure.[29] The introduction of MMT Ns led to defective sites of C_3N_5, mainly originating from the triazine ring position. To further demonstrate the formation of N defects, elemental analysis was performed on 10CN-MMT (Table S1†). In 10CN-MMT, the C/N atomic ratio was 1.16, indicating a significant decrease in N content, which confirmed the loss of lattice nitrogen and the creation of nitrogen defects in the catalyst.[19]

The presence of N-defects was further verified using ESR measurements (Fig. S2†). The Lorentz line with a *g* value of 2.003 indicated the unpaired electrons of the C atoms in the aromatic ring, which originate from the redistribution of the remaining electrons in the nitrogen loss.[31] The 10CN-MMT sample exhibited a strong symmetry signal at $g = 2.003$ in comparison with pristine C_3N_5. Thus, the reaction between the hydroxyl group on the MMT surface and the 3-amino-1,2,4-triazole intermediate during the complexation process introduced the N defects (N-d) and –C≡N group into C_3N_5. The introduction of defects promoted the electron transfer ability and reduced the reaction energy barrier for the adsorption of pollutants and PMS molecules.[7] In addition, as a typical strong electron acceptor, the –C≡N group had strong electrophilic properties that could promote electron redistribution.[32] These properties strongly influenced the subsequent adsorption and degradation performance.

In order to obtain detailed morphological information on C_3N_5, MMT Ns, and 10CN-MMT, the TEM technique was performed. As shown in Fig. 3a, the synthesized C_3N_5 displayed the morphology of fragmented agglomerates. MMT nanosheets showed a completely clear film-like morphology (Fig. 3b). TEM images of 10CN-MMT (Fig. 3c) showed that the C_3N_5 fragments were in close contact with the MMT Ns and dispersed uniformly. Fig. 3d shows the HRTEM images of the composites, and no apparent lattice fringes were found. EDS elemental mapping (Fig. 3e) shows that the C, N, Al, and Si elements in 10CN-MMT are uniformly distributed. In addition, the presence of MMT Ns induces a more dispersed feature of C_3N_5, which is conducive to improving the adsorption capability.
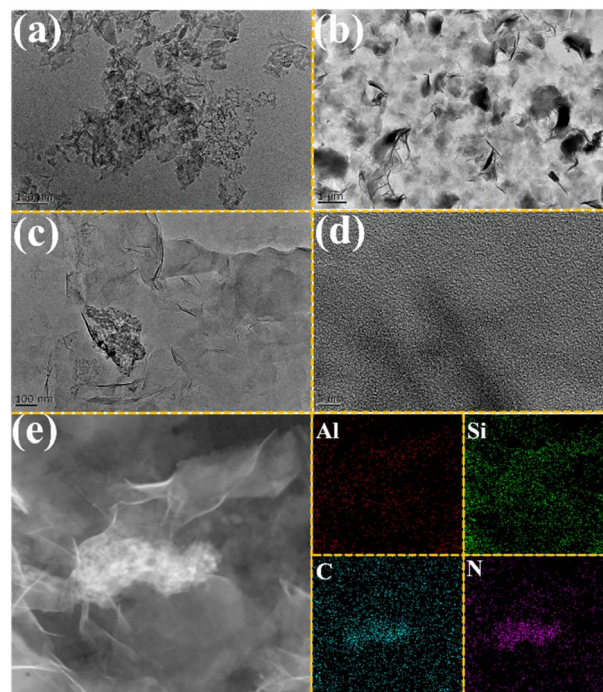

Fig. 3 TEM images of C_3N_5 (a), MMT Ns (b) and 10CN–MMT (c). HRTEM images (d) and EDS element mapping (e) of Al, Si, C, and N for 10CN–MMT.

Adsorption experiments on TC by xCN-MMT

Adsorption efficiency of TC over the samples. The adsorption properties of the synthesized samples were carried out at room temperature using tetracycline (TC) as the target pollutant. Fig. 4 shows the adsorption efficiencies of MMT, C_3N_5, and 10CN-MMT on TC, and the equilibrium of adsorption and desorption was reached within 60 min. Compared with MMT and C_3N_5, the adsorption efficiency of 10CN-MMT towards TC was improved by about 58% and 40%, respectively, which could adsorb 66% of TC within 60 min. For comparison, the physical mixture of MMT Ns and C_3N_5 (10CN + MMT) was also prepared, and the adsorption efficiency was higher than individual C_3N_5 and MMT but lower than that of 10CN-MMT. This phenomenon suggested that the 10CN-MMT adsorbent was not simply physically mixed, and the presence of MMT significantly affected the adsorption performance of C_3N_5. As shown in Fig. S3a,† the specific surface area of C_3N_5 (169 $m^2 g^{-1}$) was significantly higher than MMT Ns (26.6 $m^2 g^{-1}$) and 10CN-MMT (59.6 $m^2 g^{-1}$), and this result was not in line with the adsorption results, so the specific surface area was not the main influencing factor.

Effects of various parameters on the adsorption efficiency. In order to determine the maximum adsorption efficiency of 10CN-MMT towards TC, the effects of CN loading, catalyst dosage, TC concentration, temperature, and pH value on TC adsorption efficiency were explored. The effect of CN loading on the adsorption efficiency of TC is plotted in Fig. S4a.† The adsorption efficiency of 10CN-MMT on TC was up to 66%. However, the adsorption efficiency was not significantly improved with increasing C_3N_5 loading content. This phenomenon might be related to the limited number of exposed adsorption sites. Therefore, the 10CN-MMT sample was selected for the subsequent tests.

The effect of other parameters on the adsorption performance was also evaluated. Fig. S4b† shows the effect of 10CN-MMT dosage on the adsorption efficiency. The adsorption efficiency improved from 32% to 66% with a continuously increased adsorbent dosage. This phenomenon indicated that the increase in the sample concentration could provide a large number of adsorption sites, which was beneficial to increase the

contact between the sample and the pollutant, thus improving the adsorption performance of the sample. Fig. S4c† showed the effect of initial TC concentration on adsorption efficiency. The results showed that good adsorption efficiencies were exhibited for different concentrations of TC, with 10CN-MMT adsorbing 66% of the TC within 60 min at a TC concentration of 50 mg L^{-1}. Fig. S4d† shows the effect of temperature on the adsorption efficiency of 10CN-MMT on TC. As the temperature was increased from 0 °C to 55 °C, the adsorption efficiency was almost unchanged, indicating that the temperature had no significant effect on the TC adsorption performance. For energy saving, 25 °C was chosen as the rational temperature.

It is well known that pH value is one of the most critical parameters affecting TC adsorption efficiency and adsorbent surface charge. Thus, a series of adsorption experiments with different pH values were carried out (Fig. S4e†). The adsorption efficiency could adsorb almost 100% of TC at pH = 1–3. When the pH value was adjusted to 11, the adsorbent had almost no adsorption performance, which indicated that the alkaline condition was not favourable for the removal of TC. This result might be related to the fact that the molecular morphology of TC changes at different pH ranges (Fig. S4f†), which includes cationic species (pH < 3.3), zwitterionic species (3.3 < pH < 7.7), and anionic species (pH > 7.7).[33,34] The increase in adsorption efficiency at a pH lower than 3.3 was attributed to electrostatic adsorption between the negatively charged catalyst surface and the TC cationic species. When the pH value was above 7.7, the adsorption competition between OH^- and TC anionic species and the electrostatic repulsion between the negatively charged catalyst surface and the anionic TC appeared, which resulted in poor adsorption efficiency. As for the pH values between 3.3 and 7.7, the TC molecules as zwitterions were adsorbed on the sample surface by electrostatic interaction, the adsorption competition and electrostatic repulsion were weakened, and the adsorption capacity and adsorption efficiency were increased. Based on the above discussion, a pH value of 5 was chosen as the optimum condition for the following experiments.

Adsorption kinetics and isotherms models. Adsorption kinetic modelling is one of the most important methods for evaluating the efficiency of adsorbents. It is commonly used to study the process of adsorption of pollutants by adsorbents and the variation of adsorption rates. Four standard models, including pseudo-first-order, pseudo-second-order, Webber–Morris, and Elovich, were used to investigate the adsorption process of TC over the three samples.[35–37] The four kinetic models are represented by the following equations.

Pseudo-first-order model:

$$q_t = q_e(1 - \exp(-k_1 t)) \qquad (3)$$

where q_t (mg g^{-1}) and q_e (mg g^{-1}) represent the adsorption amount at time t and at equilibrium, respectively. The parameter k_1 (min^{-1}) is the pseudo-first-order rate constant.

Pseudo-second-order model:

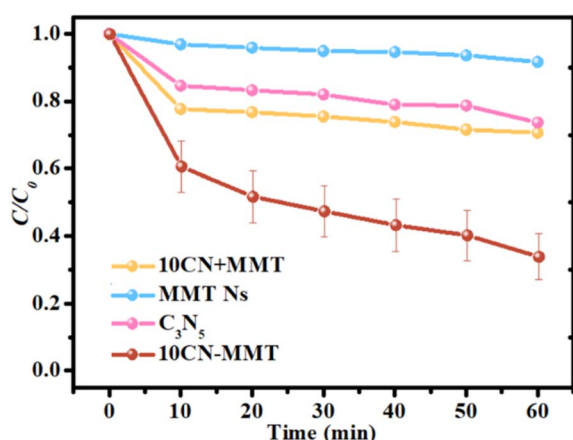$$\frac{t}{q_t} = \frac{1}{k_2 q_e^2} + \frac{1}{q_e}t \qquad (4)$$

Fig. 4 Adsorption efficiencies of TC over various samples.

© 2024 The Author(s). Published by the Royal Society of Chemistry

Environ. Sci.: Adv., 2024, **3**, 290–303 | **295**

where k_2 (mg g^{-1} h^{-1}) is the pseudo-second-order rate constant.

Webber–Morris model:

$$q_t = k_{id} \times t^{1/2} + C \tag{5}$$

where C (mg g^{-1}) is a constant. The parameter k_{id} is the internal diffusion rate constant of the adsorption method.

Elovich model:

$$q_t = \frac{1}{\beta}\ln(1 + \alpha\beta t) \tag{6}$$

where α is the initial rate constant, and β is the parameter related to the adsorbent surface coverage and chemisorption activation energy.

Kinetic data for the adsorption of TC over C$_3$N$_5$, MMT Ns, and 10CN-MMT are presented in Fig. 5 and Table S2.† As displayed in Table S2,† the pseudo-second-order and Elovich models matched well with the adsorption data, which indicated that the adsorption process of TC over C$_3$N$_5$, MMT Ns, and 10CN-MMT was more suitable for the pseudo-second-order and Elovich models. It also confirmed the inhomogeneous adsorption and interaction between TC molecules and C$_3$N$_5$, MMT Ns, and 10CN-MMT.[38] The adsorption capacity of 10CN-MMT (44.8 mg g^{-1}) was much more significant than those of MMT Ns (7.93 mg g^{-1}) and C$_3$N$_5$ (16.9 mg g^{-1}) in the pseudo-second-order kinetic adsorption model, indicating the significant role of MMT in enhancing the adsorption performance of C$_3$N$_5$.

The adsorption isotherm models could be used to study the interaction between pollutants and adsorbents at equilibrium and the distribution of adsorbed molecules at the solid–liquid interface during adsorption. Four isothermal adsorption models were chosen to fit the adsorption process of 10CN-MMT. Freundlich isothermal adsorption model: commonly used to describe the adsorption of a multimolecular layer occurring on an inhomogeneous surface, where the adsorption occurs at different locations with different adsorption energies;[39] Langmuir isothermal adsorption model: assumed that monolayer adsorption occurs on the surface of the adsorbent; Temkin isothermal model: describes the adsorbent during the adsorption of a solute, where the interaction of adsorbates generate the heat of adsorption; the Redlich–Peterson isothermal model is a combination of the Freundlich and Langmuir models.[40,41]

Langmuir model:

$$\frac{C_e}{q_e} = \frac{1}{k_L \times q_m} + \frac{C_e}{q_m} \tag{7}$$

Freundlich model:

$$\log q_e = \log k_F + \frac{1}{n}\log C_e \tag{8}$$
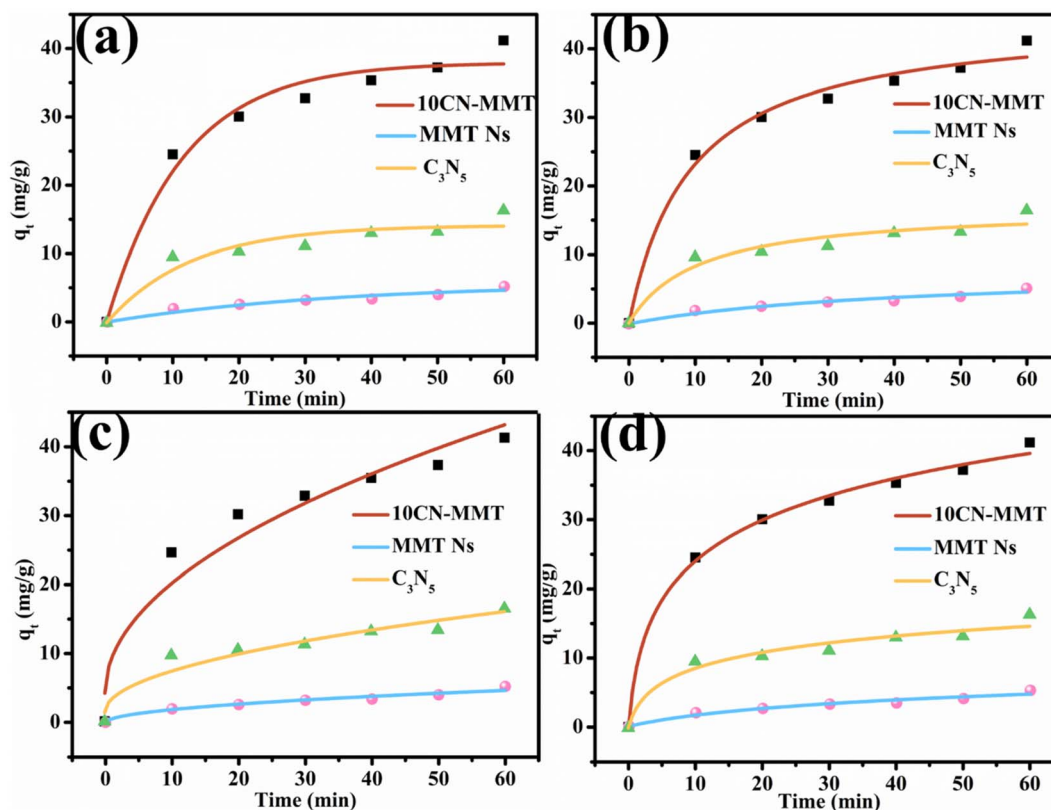
Temkin model:

$$q_e = A \ln(K_T C_e) \tag{9}$$

Fig. 5 Pseudo-first-order (a), pseudo-second-order (b), Webber–Morris (c), and Elovich (d) models for adsorption of TC over various adsorbents.

© 2024 The Author(s). Published by the Royal Society of Chemistry

Redlich–Peterson model:

$$q_e = \frac{K_p C_e}{1 + \alpha C_e} \tag{10}$$

where q_m (mg g^{-1}) is the saturation adsorption intensity; k_F, k_L, K_T and K_P (L mg^{-1}) is the adsorption rate; q_e (mg g^{-1}) and C_e (mg L^{-1}) are the saturation adsorption amount and the concentration of TC at equilibrium. n, α, and A are constants for the Freundlich, Redlich–Peterson, and Temkin models.

The data of the four adsorption models corresponding to the adsorption process of TC by adsorbent 10CN-MMT are shown in Fig. S5† and Table S3.† The fitting coefficient of Langmuir and Redlich–Peterson isothermal models, $R^2 = 0.997$, is higher than that of Freundlich ($R^2 = 0.897$) and Temkin ($R^2 = 0.972$) isothermal models. The fitting coefficients of 10CN-MMT indicate that the adsorption process of TC by 10CN-MMT is suitable for the Langmuir and Redlich–Peterson isothermal model, *i.e.*, TC molecules belong to the adsorption mode of the co-existence of monolayer adsorption and multilayer adsorption on the adsorbent 10CN-MMT.

Adsorption cycling tests. In order to check the regeneration ability and stability of adsorbent 10CN-MMT, five cycles of adsorption–desorption experiments were carried out (Fig. S6†). The results indicated that the adsorption efficiency of 10CN-MMT decreased slightly after five adsorption cycles, which could still reach about 49%, indicating that 10CN-MMT had good cycle stability for TC adsorption.

PMS activation by xCN-MMT for TC degradation

Degradation efficiency of TC over the samples. Only part of the TC could be removed by the adsorption process. To achieve a deeper treatment of the wastewater, PMS was applied for the complete degradation of TC. All prepared samples showed the performance of activated PMS toward TC degradation (Fig. S7a†). PMS was able to degrade only 29% of TC within 60 min. The 10CN-MMT catalyst showed an optimal degradation efficiency of 84%, 1.35 times higher than that of C$_3$N$_5$ (62%) and 1.29 times that of MMT Ns (65%). In order to further investigate the degradation effect of the various catalysts, first-order kinetic analysis of the degradation efficiency was performed at pH = 5, initial TC concentration = 50 mg L^{-1}, temperature = 25 °C, catalyst dosage = 0.4 g L^{-1}, and PMS concentration = 0.3 mmol L^{-1} within 60 min (Fig. S7b†). 10CN-MMT exhibited the optimal degradation rate constant (0.0218 min^{-1}). The above results indicated that the construction of 10CN-MMT played an excellent role in improving the adsorption and degradation activities of TC.

Effects of various parameters on the degradation efficiency. Fig. 6a shows TC degradation by activated PMS for samples with different CN loadings after absorption–desorption equilibrium. The results prove that all the samples could achieve high degradation efficiency within 60 min. In addition, the catalytic efficiency could be increased from 52% to 84% with increasing catalyst concentration (Fig. 6b). The increase in catalyst concentration could increase the contact opportunity between PMS molecules and the catalyst, which could promote the

catalytic activity of the catalyst. The effect of TC concentration on the catalytic activity is shown in Fig. 6c. 10CN-MMT could degrade 84% of the TC in 60 min when the TC concentration was 50 mg L^{-1}. However, the catalytic efficiency appeared to be significantly decreased with the further increase in TC concentration. This result was due to the insufficient active sites on the sample surface. As shown in Fig. 6d, the degradation efficiency increased significantly with increasing PMS concentration due to the production of more active substances. However, the increment of degradation efficiency nearly remained unchanged when the PMS concentration exceeded 0.3 mmol L^{-1}, probably due to the scavenging effect of PMS on ·OH and SO$_4^{\cdot-}$ (eqn (11)–(14)).[42]

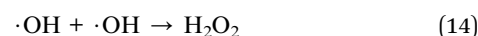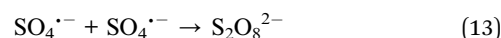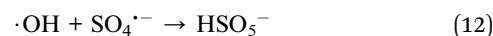$$SO_4^{\cdot-} + HSO_5^- \rightarrow SO_5^{\cdot-} + SO_4^- + H^+ \tag{11}$$

$$\cdot OH + SO_4^{\cdot-} \rightarrow HSO_5^- \tag{12}$$

$$SO_4^{\cdot-} + SO_4^{\cdot-} \rightarrow S_2O_8^{2-} \tag{13}$$

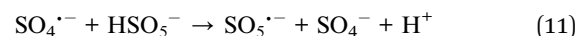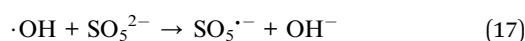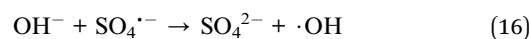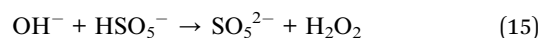$$\cdot OH + \cdot OH \rightarrow H_2O_2 \tag{14}$$

Fig. 6e shows the effect of temperature on the efficiency of TC degradation by 10CN-MMT-activated PMS. As the temperature was increased from 0 °C to 55 °C, the degradation efficiency increased slightly, indicating that the temperature had a slight effect on the TC degradation performance. The initial pH also significantly influences the activation of PMS for TC degradation. As shown in Fig. 6f, 10CN-MMT could effectively degrade TC at different pH values. When the initial pH was increased to 13, the degradation efficiency could reach 66% even though the adsorption efficiency decreased, ascribed to the consumption of ·OH, thus impeding the generation of active species (eqn (15)–(17)).[43]

$$OH^- + HSO_5^- \rightarrow SO_5^{2-} + H_2O_2 \tag{15}$$

$$OH^- + SO_4^{\cdot-} \rightarrow SO_4^{2-} + \cdot OH \tag{16}$$

$$\cdot OH + SO_5^{2-} \rightarrow SO_5^{\cdot-} + OH^- \tag{17}$$

Based on the above discussion, it was concluded that the maximum adsorption capacity was 44.8 mg g^{-1} and the maximum efficiency of activated PMS for TC degradation was 95% of sample 10CN-MMT at pH = 5, initial TC concentration = 50 mg L^{-1}, temperature = 25 °C, PMS concentration = 0.3 mmol L^{-1}, and catalyst dosage = 0.8 g L^{-1}.

The Chemical Oxygen Demand (COD) values after adsorption and degradation of TC by 10CN-MMT were tested under optimal catalytic conditions (Fig. 7a).[44] The COD values in the solution showed a significant decrease after the adsorption and degradation process, indicating a significant reduction of organic matter in the system. The total organic carbon (TOC) value of the system was tested and used to evaluate its mineralization efficiency (Fig. 7b). The TOC value of 10CN-MMT was 81.1% within 120 min when the initial TC concentration was 50 mg L^{-1}, indicating that most TC molecules had been
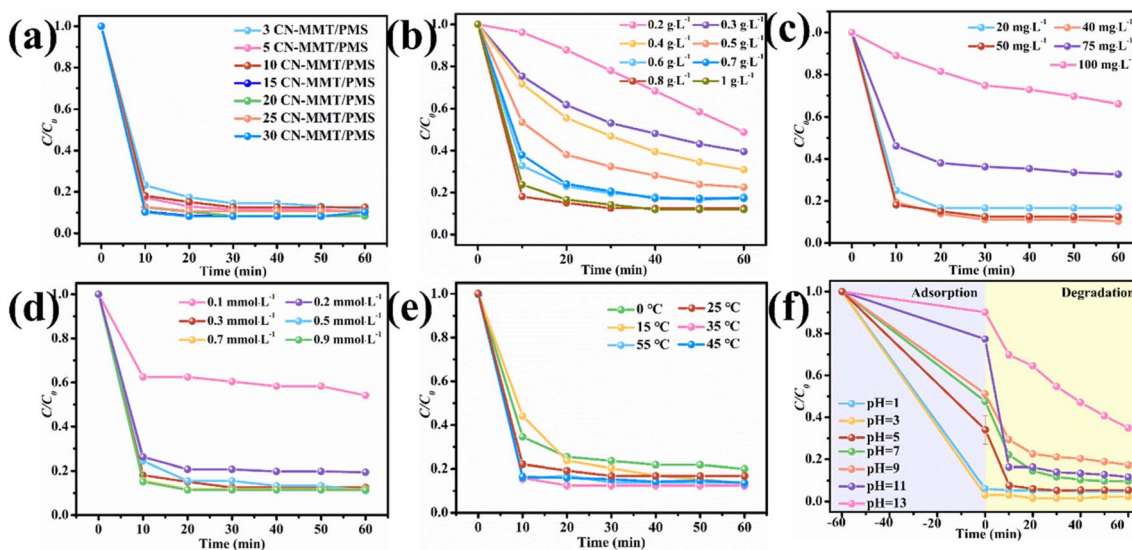
Fig. 6 Effects of CN loading amount (a), catalyst dosage (b), TC concentration (c), PMS concentration (d), temperature (e) and pH value (f) on the catalytic efficiency.

converted to CO_2 and H_2O. Table S4† summarizes the comparison of the catalytic activity of 10CN-MMT with other reported metal-free catalysts for activating PMS to degrade pollutants in water, demonstrating that 10CN-MMT is a promising catalyst for activating PMS to remove pollutants, and it could achieve a high level of mineralization efficiency for TC. Combined with FT-IR analyses (Fig. 7c), it was found that adsorption and degradation reactions occurred on the 10CN-MMT surface. Although the positions of the vibrational peaks did not change significantly after adsorption and degradation, the vibrational peaks around 2192 cm^{-1} almost disappeared after degradation. This phenomenon indicated that the –C≡N

group played a crucial role in the activation process of PMS and participated in the activation process. Because MMT surface hydroxyl groups can be removed by calcination above 700 °C, MMT was calcined at 700 and 800 °C to obtain hydroxyl-free MMT, and subsequent samples of 10CN-MMT (700, 800 °C) were prepared. The catalytic performance of 10CN-MMT (700, 800 °C) was significantly inhibited in comparison to the 10CN-MMT catalyst (Fig. S8a†). Thus, –C≡N group played a critical role in PMS activation. However, the characteristic peak of –C≡N in 10CN-MMT reappeared after treatment with alkali heat conditions, which implies that the activity could be restored by alkali heat method. To verify this result, the cycling experiment
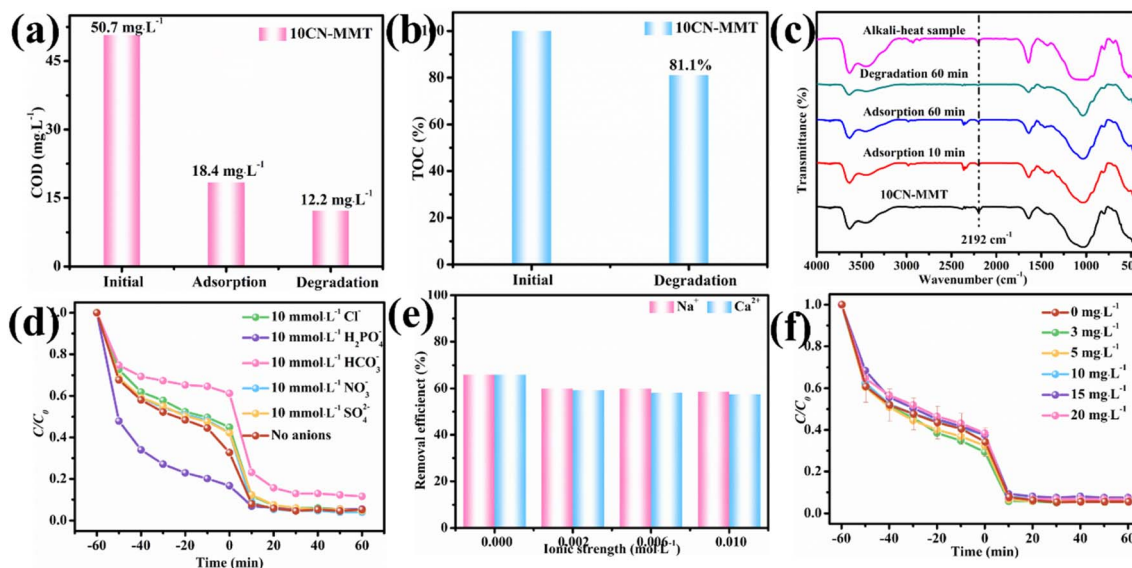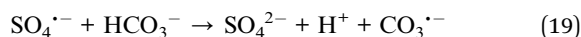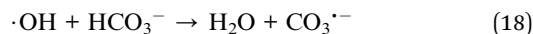

Fig. 7 COD analysis (a), TOC analysis of TC (b) and FT-IR spectra of 10CN-MMT, alkali-heat sample, and reclaimed samples after adsorption and degradation (c). Effects of inorganic ions (d), ionic strength for Ca^{2+} and Na^+ (e), and concentration of humic acid (f) on the removal efficiency of TC over 10CN-MMT. General experiment parameters: [TC] = 50 mg L^{-1}; [10CN-MMT] = 0.8 g L^{-1}; [PMS] = 0.3 mmol L^{-1}; initial pH = 5.0; T = 25 °C.

was performed (Fig. S8b†). 10CN-MMT exhibited a slight decrease in degradation efficiency after 5 cycles, which indicated that the catalyst 10CN-MMT had excellent recyclability. Fig. S8c† shows the XRD pattern of the 10CN-MMT after-reaction and alkaline-heated samples. The crystallinity of the sample decreased after the reaction but improved significantly after alkaline heat treatment. Thus, the decrease in the intensity of the vibrational peak at 2192 cm^{-1} of the alkaline-heated sample was the main reason for the decrease in the catalytic performance. Since the –C≡N group played a critical role in PMS activation, the reduction of –C≡N might affect the catalytic reactivity and cause a decrease in TC degradation efficiency.

The groundwater usually contains many different anions, such as Cl$^-$, H$_2$PO$_4^-$, HCO$_3^-$, and SO$_4^{2-}$, which also could scavenge free radicals in the process of AOPs. Thus, the effect of different anions on the removal of TC by 10CN-MMT was investigated (Fig. 7d). SO$_4^{2-}$, Cl$^-$, and NO$_3^-$ slightly affected the adsorption efficiency, which might be due to competitive adsorption with TC molecules. On the other hand, H$_2$PO$_4^-$ was more ionized than hydrolysed, generating more H$^+$ and contributing to a lower solution pH, which made adsorption more likely to occur. The ability of HCO$_3^-$ to bind hydrogen ions was more significant than its ability to ionize hydrogen ions, so the solution was alkaline and inhibited the adsorption of TC by 10CN-MMT. In addition, HCO$_3^-$ could also react with SO$_4^{\bullet-}$ or ·OH to form CO$_3^{\bullet-}$ with lower oxidation capacity (eqn (18) and (19)).[5]

$$·OH + HCO_3^- \rightarrow H_2O + CO_3^{\bullet-} \tag{18}$$

$$SO_4^{\bullet-} + HCO_3^- \rightarrow SO_4^{2-} + H^+ + CO_3^{\bullet-} \tag{19}$$

In addition, various metal ions and macromolecular organics were present in the wastewater, Ca^{2+} and Na$^+$ as metal ions, and humic acid (HA) as macromolecular organics were selected to evaluate the pollutant removal ability of 10CN-MMT. As shown in Fig. 7e, when the ion concentration was increased from 0 to 0.01 mol L^{-1}, the adsorption performance of 10CN-MMT was almost unaffected by Na$^+$ and Ca^{2+} and only slightly decreased. The reason could be attributed to the fact that the presence of Ca^{2+} and Na$^+$ would occupy the active sites of the adsorbent, leading to adsorption competition between TC molecules and metal ions. Besides, the presence of metal ions might affect the surface charge of 10CN-MMT, which weakened the interaction between TC molecules and adsorbent, resulting in electrostatic repulsion.[39] The influence of Ca^{2+} in these two aspects was more significant than that of Na$^+$, so the presence of Ca^{2+} had a more significant effect on the adsorption performance of 10CN-MMT. Fig. 7f shows the effect of different concentrations of humic acid (HA) on TC adsorption efficiency. The adsorption and degradation efficiencies were hardly affected when humic acid concentration was increased from 0 to 20 mg L^{-1}.

To investigate the general applicability of the 10CN-MMT catalyst further, different water sources and various pollutants were selected as degradation targets. Deionized water, tap

water, river water (Dahei River, Hohhot), reclaimed water (Xiaohei River, Hohhot), and lake water (Nan Lake, Hohhot) were chosen to simulate the aqueous environment in real applications (Fig. S9a†). The results showed that the 10CN-MMT catalyst could effectively degrade TC in different water environments at a low catalyst dosage. The pH test of different water samples displayed neutrality. Thus, the improved performance might be related to the presence of various ions in the solution. This result indicated that the synthesized catalysts were highly adaptable. As shown in Fig. S9b,† the degradation efficiencies of 10CN-MMT for 2,4-p-nitrophenol (2,4-DCP), ciprofloxacin (CIP), and oxytetracycline (OTC) in the range of 50 mg L^{-1} were 45%, 99%, and 84%, respectively. The results showed that 10CN-MMT exhibited significant removal effects for phenolic compounds and antibiotics, especially antibiotics that could achieve high removal efficiencies. Thus, it had good applicability in removing various pollutants.

Possible degradation pathways of TC and toxicological analysis. The possible intermediates of TC were identified by LC-MS tests (Fig. S10 and Table S5†). Furthermore, the possible degradation pathways of TC removal are shown in Fig. 8. In path I, the TC molecule was attacked by O$_2^{\bullet-}$ to produce the **P1** (m/z = 428) intermediate by the dehydroxylation reaction, which continued to be converted to **P2** (m/z = 362) by the demethylation reaction and deamidation reaction. Subsequently, the ring was opened by a dehydroxylation reaction to produce **P3** (m/z = 318).[45] In degradation pathway II, the TC molecule was attacked by SO$_4^{\bullet-}$ and ^{1}O$_2$ and was demethylated and dihydroxylated to produce **P4** (m/z = 415), which was further demethylated to form **P5** (m/z = 400). Then, **P5** molecule was gradually ring-opened and delocalized to produce **P6** (m/z = 445), which was further hydroxylated to produce **P7** (m/z = 274).[46] In pathway III, the TC molecule (m/z = 445) was hydroxylated by ·OH and SO$_4^{\bullet-}$ to form **P8** (m/z = 460), which would be attacked by O$_2^{\bullet-}$ and ^{1}O$_2$ and undergo benzene ring cleavage to convert to **P9** (m/z = 218), followed by the removal of the carboxyl group and the ring opening of **P10** (m/z = 174) into small molecules.[47] In addition, **P3**, **P7**, and **P10** intermediates could be further oxidized to produce intermediates, including **P11–P15** compounds, a class of low molecular weight organics, which significantly reduces biotoxicity. Then, the small molecular organics were decomposed to CO$_2$ and H$_2$O under the continuous attack of the active species.

The mutagenicity value, acute toxicity LC50 of fathead minnow, and acute toxicity LC50 of *Daphnia magna* of TC and its intermediate products were analysed by employing the Toxicity Estimation Software Tool (T.E.S.T.) according to quantitative structure–activity relation (QSAR) prediction (Fig. S11†).[48,49] According to the prediction in Fig. S11a,† some of the intermediates were still positive for mutagenicity, but the mutagenicity values of the final products were mostly reduced to negative. The LC50 (LC50 after 96 h) of TC for Fathead minnow was 0.9 mg L^{-1}, implying that TC was very toxic. Most of the degradation products had higher LC50s, reflecting that the acute toxicity of the TC solution was significantly reduced by degradation (Fig. S11b†). Similarly, in Fig. S11c,† the LC50s of almost all intermediates for *Daphnia magna* were lower than
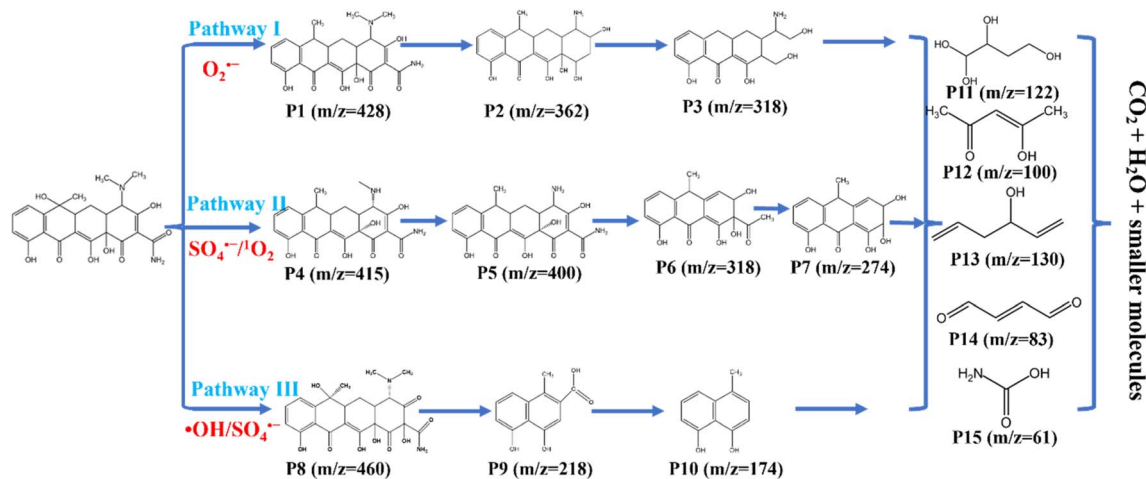
© 2024 The Author(s). Published by the Royal Society of Chemistry

Environ. Sci.: Adv., 2024, **3**, 290–303 | **299**

Fig. 8 The possible degradation pathways of TC in the 10CN–MMT/PMS system.

that of TC (5.44 mg L^{-1}) except **P5**, **P1**, and **P4**, indicating that the toxicity of the TC solution has been dramatically reduced after degradation. The above toxicity prediction results indicated that the 10CN-MMT catalyst could effectively degrade TC and reduce the overall toxicity of TC during PMS activation.

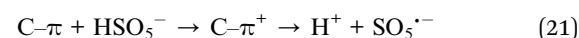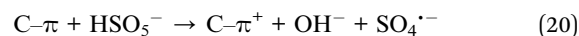### Catalytic mechanism analyses

Exploration of active species. In order to further explore the process of pollutant degradation by 10CN-MMT, the active species involved in the degradation process were verified by quenching tests. Methanol (MeOH) could be used as a free radical scavenger to quench SO$_4^{\bullet-}$ and ·OH ($k_{SO_4^{\bullet-}} = 1.6$–$7.7 \times 10^7$ M^{-1} s^{-1}, $k_{·OH} = 1.2$–2.8×10^9 M^{-1} s^{-1}). Tertiary butyl alcohol (TBA) captured ·OH ($k_{·OH} = 3.8$–7.6×10^8 M^{-1} s^{-1}) at a significantly higher reaction rate than SO$_4^{\bullet-}$ ($k_{SO_4^{\bullet-}} = 4.0$–$9.1 \times 10^5$ M^{-1} s^{-1}), thus it could be used to capture ·OH.[50] However, as shown in Fig. 9a, when 1 mmol L^{-1} of MeOH and TBA were added to the system, the catalytic efficiency decreased from 84% to 79% and 83%. ^{1}O$_2$ and O$_2^{\bullet-}$ were also common reactive species during PMS activation. The effects of sodium azide (NaN$_3$),[51] L-histidine (L-his) and 1,4-benzoquinone (p-BQ) on the degradation efficiency of the 10CN-MMT/PMS system is also shown in Fig. 9a. When 1 mmol L^{-1} of L-his, NaN$_3$ and p-BQ were added to the system, the catalytic efficiency decreased to 61%, 62%, and 33%, respectively. Thus, it could be assumed that SO$_4^{\bullet-}$, ^{1}O$_2$, and O$_2^{\bullet-}$ active species were involved in the reaction.

ESR analysis was conducted to demonstrate further the active species produced during the activation of PMS by 10CN-MMT. As shown in Fig. S12,† no peaks were observed in the PMS system with the addition of DMPO and TEMP, which meant that PMS could not produce the active species alone without a catalyst. As shown in Fig. 9b–d, the 10CN-MMT and 10CN-MMT/PMS systems were compared. The catalyst alone could also not produce active species to degrade the pollutants and thus adsorb the pollutants. However, after using 10CN-MMT to activate PMS, distinct characteristic peaks appeared. It proved that active species ·OH, SO$_4^{\bullet-}$, ^{1}O$_2$, and O$_2^{\bullet-}$ were present in the

10CN-MMT system. In addition, ·OH might be converted to SO$_4^{\bullet-}$ and thus not easily quenched by TBA.[52,53]

The possible catalytic mechanism. During the thermal polymerization of 3-amino-1,2,4-triazole, the rich hydroxyl group in MMT could react with the amino group in the intermediate to form the –C≡N.[19,54] In addition, the rapid evaporation of water molecules during the thermal polymerization of 3-amino-1,2,4-triazolen might limit the long-range ordered polymerization process of 3-amino-1,2,4-triazole, resulting in the generation of nitrogen vacancies. This was the reason for the presence of defect signals in C$_3$N$_5$. MMT Ns not only played a role in dispersing C$_3$N$_5$, but the surface hydroxyl groups also promoted the formation of –C≡N and nitrogen defects in the catalyst. –C≡N (edge defects) and N defects are two typical defect structures. The presence of defects could serve as adsorption sites to promote the adsorption of TC, PMS, and O$_2$ molecules.[7,13] According to previous reports, in carbon-based non-metallic materials, defects could contribute to the formation of a large number of off-domain π-electrons (C–π) on the surface of the material, which could act as electron donors for transferring electrons to PMS molecules, promoting the conversion of PMS to active species.[55] The O–O bonds in the PMS molecule broke to form SO$_4^{\bullet-}$ and SO$_5^{\bullet-}$. SO$_5^{\bullet-}$ was unstable and decomposed to produce SO$_4^{\bullet-}$ and O$_2$ molecules. SO$_4^{\bullet-}$ and ·OH could be converted into each other to produce the reactive species continuously. Both SO$_5^{\bullet-}$ and defective sites could produce ^{1}O$_2$. O$_2$ molecules were attacked by electrons and converted to O$_2^{\bullet-}$. Finally, the active species ·OH, SO$_4^{\bullet-}$, ^{1}O$_2$, and O$_2^{\bullet-}$ oxidatively decompose the TC into several intermediates until mineralization into CO$_2$ and H$_2$O.

Based on the reported studies and the above analysis of active species, the proposed mechanism for the study of TC removal by 10CN-MMT activated PMS is shown in Fig. 10 and eqn (20)–(28) as follows.
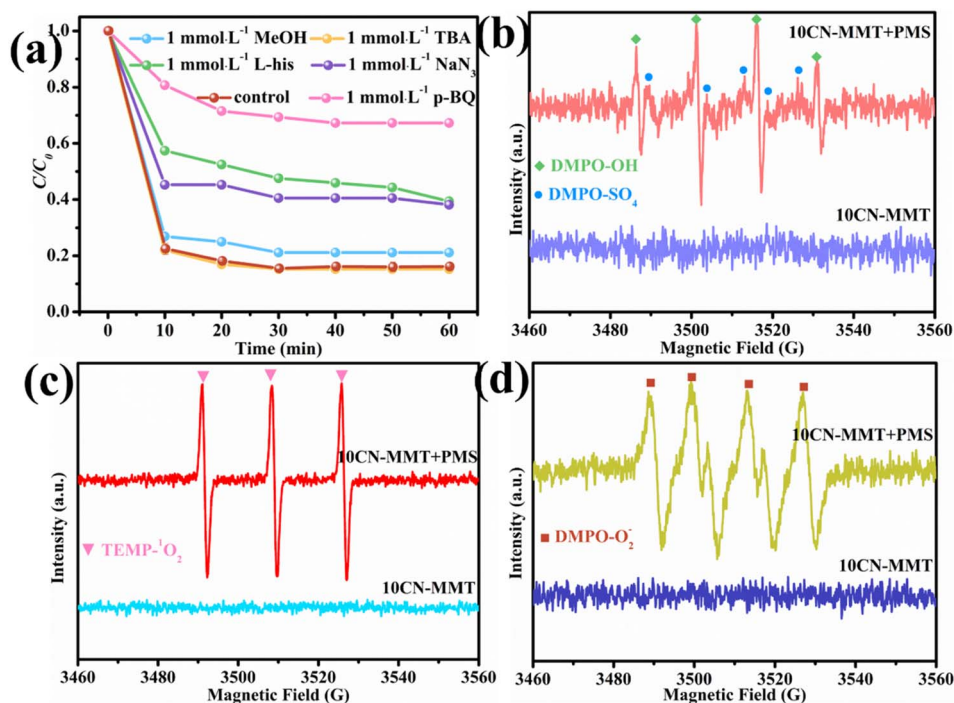
$$C–π + HSO_5^- \rightarrow C–π^+ + OH^- + SO_4^{\bullet-} \quad (20)$$

$$C–π + HSO_5^- \rightarrow C–π^+ \rightarrow H^+ + SO_5^{\bullet-} \quad (21)$$

300 | *Environ. Sci.: Adv.*, 2024, **3**, 290–303

© 2024 The Author(s). Published by the Royal Society of Chemistry

Fig. 9 The catalytic efficiency of TC in the presence of various scavengers (a). ESR spectra of DMPO-OH and DMPO-SO$_4$ (b), TEMP-^{1}O$_2$ (c), and DMPO-O$_2^{\cdot-}$ (d) adducts in 10CN-MMT and 10CN-MMT + PMS systems with the reaction time of 5 min.
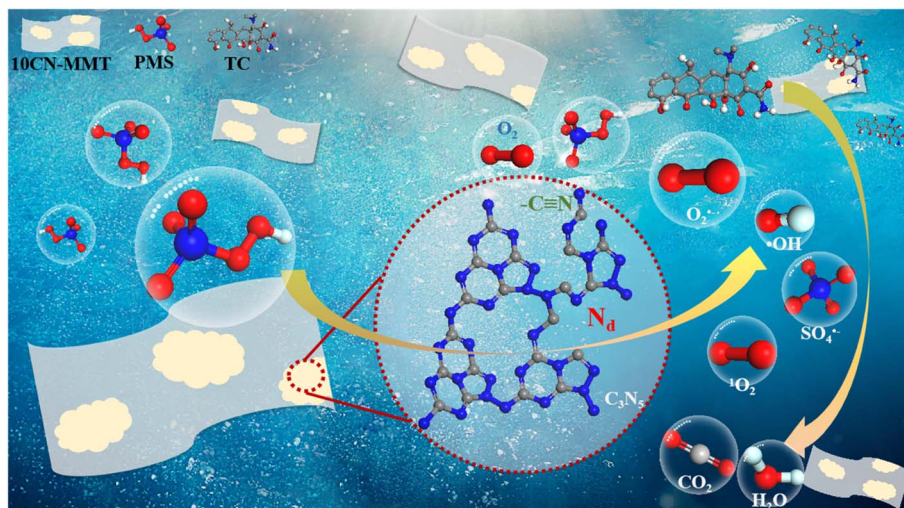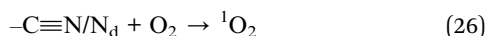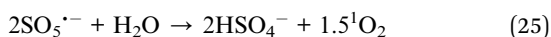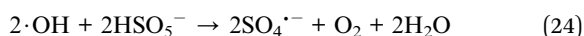

Fig. 10 The schematic diagram of the proposed mechanism for TC removal by 10CN-MMT.

$$2SO_5^{\cdot-} \rightarrow 2SO_4^{\cdot-} + O_2 \quad (22)$$

$$SO_4^{\cdot-} + H_2O \rightarrow SO_4^{2-} + \cdot OH + H^+ \quad (23)$$

$$2\cdot OH + 2HSO_5^- \rightarrow 2SO_4^{\cdot-} + O_2 + 2H_2O \quad (24)$$

$$2SO_5^{\cdot-} + H_2O \rightarrow 2HSO_4^- + 1.5^1O_2 \quad (25)$$

$$-C\equiv N/N_d + O_2 \rightarrow {}^1O_2 \quad (26)$$

$$O_2 + e^- \rightarrow O_2^{\cdot-} \quad (27)$$

$$TC + SO_4^{\cdot-}/\cdot OH/O_2^{\cdot-}/{}^1O_2 \rightarrow \text{intermediates} \rightarrow CO_2 + H_2O \quad (28)$$
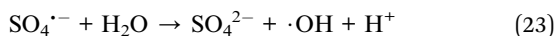
Conclusions

In summary, a series of composite catalysts (*x*CN-MMT) were prepared by thermal polymerization. By adjusting the experimental parameters, 10CN-MMT showed better performance in adsorption (maximum adsorption 44.8 mg g^{-1}) and degradation (95%) performance. The enhanced adsorption and catalytic

© 2024 The Author(s). Published by the Royal Society of Chemistry

Environ. Sci.: Adv., 2024, **3**, 290–303 | **301**

activities were mainly attributed to the hydroxyl groups on the surface of MMT that contributed to the creation of double defect sites (–C≡N and N defects) in the composite samples. The formation of the defects promotes the adsorption of TC, PMS, and O_2 molecules and promotes the generation of reactive species. ESR and quenching experiments demonstrated that $\cdot OH$, $SO_4^{\cdot-}$, $^1O_2$, and $O_2^{\cdot-}$ participated in the reaction. The LC-MS technique analysed the intermediates of the TC degradation process, and possible degradation pathways and catalytic mechanisms were proposed in combination with the active species. In this study, we explored the activation mechanism of PMS by metal-free clay-based catalysts for pollutant removal, which provided a new efficient catalyst and broadened the application pathway of clay-based materials.

Author contributions

Min Li: designed the experiments, wrote the original manuscript, gave some suggestions, and made deep discussion. Xudong Liu, Zhinan Xie: gave some suggestions and made deep discussion. Chunfang Du: made deep discussion and revised the manuscript. Yiguo Su: conceptualization, supervision, made deep discussion and revised the manuscript. All authors discussed the results and commented on the manuscript.

Conflicts of interest

The authors declare that they have no known competing financial interests that could have appeared to influence the work reported in this paper.

Acknowledgements

References

1 L. Zhou, S. M. Limbu, M. Shen, W. Zhai, F. Qiao, A. He, Z.-Y. Du and M. Zhang, *Environ. Pollut.*, 2018, **235**, 245–254.

2 C. B. Özkal, D. Venieri, I. Gounaki and S. Meric, *Appl. Catal., B*, 2019, **244**, 612–619.

3 D. L. Cheng, H. H. Ngo, W. S. Guo, Y. W. Liu, J. L. Zhou, S. W. Chang, D. D. Nguyen, X. T. Bui and X. B. Zhang, *Sci. Total Environ.*, 2018, **621**, 1664–1682.

4 J. Jin, Z. Yang, W. Xiong, Y. Zhou, R. Xu, Y. Zhang, J. Cao, X. Li and C. Zhou, *Sci. Total Environ.*, 2019, **650**, 408–418.

5 S. Qu, W. Wang, X. Pan and C. Li, *J. Hazard. Mater.*, 2020, **384**, 121494.

6 M. Li, H. Zhang, Z. Liu, Y. Su and C. Du, *Appl. Surf. Sci.*, 2023, **628**, 157302.

7 M. Li, H. Zhang, Z. Liu, Y. Su and C. Du, *Chem. Eng. J.*, 2020, **450**, 138147.

8 W. Zhang, L. Zhou and H. Deng, *J. Mol. Catal. A: Chem.*, 2016, **423**, 270–276.

9 C. Guan, J. Jiang, S. Pang, X. Chen, R. D. Webster and T.-T. Lim, *Chem. Eng. J.*, 2020, **387**, 123726.

10 C. Liu, J. Zhang and W. Wang, *Surf. Interfaces*, 2023, **42**, 103491.

11 P. Kumar, E. Vahidzadeh, U. K. Thakur, P. Kar, K. M. Alam, A. Goswami, N. Mahdi, K. Cui, G. M. Bernard, V. K. Michaelis and K. Shankar, *J. Am. Chem. Soc.*, 2019, **141**, 5415–5436.

12 C. Fu, T. Wu, G. Sun, G. Yin, C. Wang, G. Ran and Q. Song, *Appl. Catal., B*, 2023, **323**, 122196.

13 C. Fu, M. Zhao, X. Chen, G. Sun, C. Wang and Q. Song, *Appl. Catal., B*, 2023, **332**, 122752.

14 Z. Ai, Y. Zhao, R. Gao, L. Chen, T. Wen, W. Wang, T. Zhang, W. Ge and S. Song, *J. Cleaner Prod.*, 2022, **357**, 132000.

15 J. Wang, W. Wang, Z. Ai, M. Li, H. Li, W. Peng, Y. Zhao and S. Song, *Appl. Clay Sci.*, 2021, **210**, 106153.

16 T. Chen, Y. Yuan, Y. Zhao, F. Rao and S. Song, *Langmuir*, 2019, **35**, 2368–2374.

17 L. Zhong, S. Hu, X. Yang, M. Yang, T. Zhang, L. Chen, Y. Zhao and S. Song, *Colloids Surf., A*, 2021, **617**, 126364.

18 X. Liu, W. Wang, C. Du and Y. Su, *Appl. Clay Sci.*, 2022, **228**, 106625.

19 X. Zhang, R. Zhao, N. Zhang, Y. Su, Z. Liu, R. Gao and C. Du, *Appl. Catal., B*, 2020, **263**, 118316.

20 H. Wang, M. Li, Q. Lu, Y. Cen, Y. Zhang and S. Yao, *ACS Sustainable Chem. Eng.*, 2018, **7**, 625–631.

21 J. Zhang, B. Jing, Z. Tang, Z. Ao, D. Xia, M. Zhu and S. Wang, *Appl. Catal., B*, 2021, **289**, 120023.

22 Q. Han, B. Wang, J. Gao and L. Qu, *Angew. Chem., Int. Ed.*, 2016, **55**, 10849–10853.

23 B. V. Lotsch, M. Döblinger, J. Sehnert, L. Seyfarth, J. Senker, O. Oeckler and W. Schnick, *Chem. - Eur. J.*, 2007, **13**, 4969–4980.

24 J. Temuujin, T. Jadambaa, G. Burmaa, S. Erdenechimeg, J. Amarsanaa and K. J. D. MacKenzie, *Ceram. Int.*, 2004, **30**, 251–255.

25 P. M. Amarasinghe, K. S. Katti and D. R. Katti, *J. Colloid Interface Sci.*, 2009, **337**, 97–105.

26 V. W.-h. Lau, I. Moudrakovski, T. Botari, S. Weinberger, M. B. Mesch, V. Duppel, J. Senker, V. Blum and B. V. Lotsch, *Nat. Commun.*, 2016, **7**, 12165.

27 W. Zhang, L. Wang, Y. Su, Z. Liu and C. Du, *Appl. Surf. Sci.*, 2021, **566**, 150708.

28 Y. Xing, X. Gao, G. Ji, Z. Liu and C. Du, *Appl. Surf. Sci.*, 2019, **465**, 369–382.

29 G. P. Mane, S. N. Talapaneni, K. S. Lakhi, H. Ilbeygi, U. Ravon, K. Al-Bahily, T. Mori, D. H. Park and A. Vinu, *Angew. Chem., Int. Ed.*, 2017, **56**, 8481–8485.

30 W. Wu, J. Zhang, W. Fan, Z. Li, L. Wang, X. Li, Y. Wang, R. Wang, J. Zheng, M. Wu and H. Zeng, *ACS Catal.*, 2016, **6**, 3365–3371.

31 S. Zhang, S. Song, P. Gu, R. Ma, D. Wei, G. Zhao, T. Wen, R. Jehan, B. Hu and X. Wang, *J. Mater. Chem. A*, 2019, **7**, 5552–5560.

32 X. Liu, P. Wang, H. Zhai, Q. Zhang, B. Huang, Z. Wang, Y. Liu, Y. Dai, X. Qin and X. Zhang, *Appl. Catal., B*, 2018, **232**, 521–530.

33 Z. Li, L. Schulz, C. Ackley and N. Fenske, *J. Colloid Interface Sci.*, 2010, **351**, 254–260.

34 P. Zhang, R. Zhao, Z. Liu, Y. Su and C. Du, *New J. Chem.*, 2023, **47**, 6685–6693.

35 M. Chen, Z. Wang, Y. Liu, J. Chen, J. Liu and D. Gan, *J. Mater. Sci.*, 2020, **56**, 2979–2993.

36 A. Alshameri, A. Ibrahim, A. M. Assabri, X. Lei, H. Wang and C. Yan, *Powder Technol.*, 2014, **258**, 20–31.

37 T. Brudey, L. Largitte, C. Jean-Marius, T. Tant, P. C. Dumesnil and P. Lodewyckx, *J. Anal. Appl. Pyrolysis*, 2016, **120**, 450–463.

38 H. Zhang, R. Zhao, Z. Liu, X. Zhang and C. Du, *Appl. Clay Sci.*, 2023, **231**, 106730.

39 H. Zhang, P. Zhang, Z. Liu and C. Du, *J. Mol. Struct.*, 2023, **1289**, 135918.

40 L. Zhang, W. Xue and L. Gu, *Cellulose*, 2019, **26**, 5583–5601.

41 P. Li, Y.-J. Su, Y. Wang, B. Liu and L.-M. Sun, *J. Hazard. Mater.*, 2010, **179**, 43–48.

42 L. Chen, X. Zuo, L. Zhou, Y. Huang, S. Yang, T. Cai and D. Ding, *Chem. Eng. J.*, 2018, **345**, 364–374.

43 Y.-H. Guan, J. Ma, X.-C. Li, J.-Y. Fang and L.-W. Chen, *Environ. Sci. Technol.*, 2011, **45**, 9308–9314.

44 M. Li, Z. He, H. Zhong, W. Sun, L. Hu and M. Luo, *Chem. Eng. J.*, 2022, **441**, 136024.

45 Y. Luo, A. Zheng, J. Li, Y. Han, M. Xue, L. Zhang, Z. Yin, C. Xie, Z. Chen, L. Ji, Z. Hong and X. Xie, *Chem. Eng. J.*, 2023, **457**, 141228.

46 L. Liu, M. Yu, Y. Li, C. Han, G. Ding, S. Liu, Y. Xie and J. Liu, *Sep. Purif. Technol.*, 2022, **295**, 121358.

47 F. Wang, Z. Bian, W. Zhang, L. Zheng, Y. Zhang and H. Wang, *Sep. Purif. Technol.*, 2023, **314**, 123549.

48 S. Li, C. Wang, Y. Liu, M. Cai, Y. Wang, H. Zhang, Y. Guo, W. Zhao, Z. Wang and X. Chen, *Chem. Eng. J.*, 2022, **429**, 132519.

49 J. Liu, L. Huang, Y. Li, J. Shi and H. Deng, *Environ. Pollut.*, 2023, **329**, 121645.

50 W. Zhang, X. Yan, Z. Liu and C. Du, *Appl. Clay Sci.*, 2022, **224**, 106509.

51 C. Su, R. Li, C. Li and W. Wang, *Appl. Catal., B*, 2022, **310**, 121330.

52 W. Tong, Y. Xie, H. Luo, J. Niu, W. Ran, W. Hu, L. Wang, C. Yao, W. Liu, Y. Zhang and Y. Wang, *Chem. Eng. J.*, 2019, **378**, 122187.

53 C. Su, C. Li and W. Wang, *Rare Met.*, 2023, **42**(12), 4005–4014.

54 Q. Zhao, L. Fu, D. Jiang, Y. Xi and H. Yang, *MedChemComm*, 2018, **54**, 8249–8252.

55 W.-D. Oh, Z. Dong and T.-T. Lim, *Appl. Catal., B*, 2016, **194**, 169–201.

© 2024 The Author(s). Published by the Royal Society of Chemistry

Environ. Sci.: Adv., 2024, **3**, 290–303 | **303**